



de Grouchy, C. J. L., Sanloup, C., Cochain, B., Drewitt, J. W. E., Kono, Y., & Crépisson, C. (2017). Lutetium incorporation in magmas at depth: changes in melt local environment and the influence on partitioning behaviour. *Earth and Planetary Science Letters*, 464, 155-165.
<https://doi.org/10.1016/j.epsl.2017.02.017>

Peer reviewed version

Link to published version (if available):
[10.1016/j.epsl.2017.02.017](https://doi.org/10.1016/j.epsl.2017.02.017)

[Link to publication record in Explore Bristol Research](#)
PDF-document

This is the author accepted manuscript (AAM). The final published version (version of record) is available online via Elsevier at <http://www.sciencedirect.com/science/article/pii/S0012821X17300857> . Please refer to any applicable terms of use of the publisher.

University of Bristol - Explore Bristol Research

General rights

This document is made available in accordance with publisher policies. Please cite only the published version using the reference above. Full terms of use are available:
<http://www.bristol.ac.uk/pure/about/ebr-terms>

Lutetium incorporation in magmas at depth: changes in melt local environment and the influence on partitioning behaviour

Charlotte J. L. de Grouchy^{1*}, Chrystèle Sanloup², Benjamin Cochain², James W. E. Drewitt³, Yoshio Kono⁴, Céline Crépeisson²

¹*Centre for Science at Extreme Conditions and School of Physics and Astronomy, University of Edinburgh, EH9 3FD, UK. *Corresponding author (c.degrouchy@ed.ac.uk).*

²*Sorbonne Universités, UPMC Univ Paris 06, CNRS, Institut des Sciences de la Terre de Paris (ISTeP), 75005 Paris, France*

³*School of Earth Sciences, University of Bristol, Wills Memorial Building, Queens Road, Bristol, BS8 1RJ, UK.*

⁴*HPCAT, Geophysical Laboratory, Carnegie Institution of Washington, USA*

Abstract

The structure of two Lu doped (4000 ppm) model end member silicate liquids, a highly polymerised haplogranite (Si-Al-Na-K-O) and a less polymerised anorthite-diopside (Si-Al-Mg-Ca-O), have been studied up to 8 GPa using *in situ* x-ray diffraction techniques. The results are the first to identify trace rare Earth element incorporation in silicate melts at high pressure. At pressures below 5 GPa, the bonding environment of Lu-O was found to be dependent on composition with coordination number $CN_{\text{Lu-O}} = 8$ and bond distance $r_{\text{Lu-O}} = 2.36 \text{ \AA}$ in the haplogranite melt, decreasing to $CN_{\text{Lu-O}} = 6$ and $r_{\text{Lu-O}} = 2.29 \text{ \AA}$ in the anorthite-diopside melt. This compositional variance in coordination number at low pressure is consistent with observations made for Y-O in glasses at ambient conditions and is coincident with a dramatic increase in the partition coefficients previously observed for rare Earth elements with increasing melt polymerisation. With increasing pressure we find that $CN_{\text{Lu-O}}$ and $r_{\text{Lu-O}}$ remain constant in the haplogranite melt. However, an abrupt change in both Lu-O coordination and bond distance is observed at 5 GPa in the anorthite-diopside melt, with $CN_{\text{Lu-O}}$ increasing from 6 to 8-fold and $r_{\text{Lu-O}}$ from 2.29 to 2.39 \AA . This occurs over a similar pressure range where a change in the P-dependence in the reported rare Earth element partition coefficients is observed for garnet-, clinopyroxene-, and olivine-melt systems. This work shows that standard models for predicting trace elements at depth must incorporate the effect of pressure-induced structural transformations in the melt in order to realistically predict partitioning behaviour.

1. Introduction

Trace elements are highly fractionated during planetary differentiation events, because of differential partitioning between minerals, melts and metals at high pressures (P) and temperatures (T). The resulting partition coefficients are used as key indicators of depth, temperature, composition and potential age of melting events since planetary formation (McIntire (1963)). Trace element partitioning behaviour at mantle pressures is of particular interest for dating early crust formation on Earth and the Lu/Hf isotope system is regularly used to constrain early Earth melting processes (Guitreau et al. (2012)). Many studies have shown that variables such as composition, P , T and oxygen fugacity have a control on the mineral/melt partitioning of trace elements (see Wood and Blundy (2013) and references within). Although it has long been recognised that crystal chemistry and composition play a major role in controlling how elements partition (Blundy and Wood, 1994), fewer studies have focused on the influence of the melt structure due to the lack of systematic experimental data (Corgne et al., 2012).

Variations in the melt however do influence partitioning significantly, as first reported by several compositional studies, e.g. olivine/melt Ni partitioning (Hart and Davis, 1978), rare earth elements (REEs) partitioning between granitic and gabbroic melts (Ryerson and Hess, 1978; Schmidt et al., 2006), REE clinopyroxene/melt partitioning (Gaetani, 2004), titanite/melt trace element partitioning (Prowatke and Klemme, 2005), REE forsterite/melt partitioning (Evans et al., 2008). As the polymerisation of the melt was increased, a two orders of magnitude increase in partition coefficient for trivalent rare earth elements such as Lu, Y, La, is observed with high field strength elements (HFSE) such as Hf and Zr unaffected (Prowatke and Klemme, 2005; Schmidt et al., 2006). Prowatke and Klemme (2005) concluded that the polymerisation of the melt reduces the number of non-bridging oxygens available to bond with the trivalent cations, resulting in a preference for REEs to enter less polymerised melt structures. This was confirmed by a molecular dynamic study of Y in silicate melts (Haigis et al., 2013), that demonstrated the greater affinity of Y for Ca than for Si or Al in depolymerized melts, due to the weaker nature of the Ca-O bond compared to the Si(Al)-O bonds, resulting in more non-bridging oxygens being effectively available for Y. If pressure also has a significant effect on the melt structure and influence the compatibility of elements, then our current perception of how these element pairs behave at the conditions of melting may be altered.

To predict partitioning ratios, current models are based on experimental data for

35 partition coefficients measured within individual systems and extrapolated for different
36 size and charge of cations. One model that is frequently used to predict partitioning
37 ratios is the ‘lattice strain model’ (Blundy and Wood, 1994). This incorporates the
38 effect of ionic radius, charge and cation size in a model that links the parabolic relation
39 between the partition coefficient and ionic radius with the size of the ion and Young’s
40 modulus or elasticity of the lattice site. No explicit term for the effect of melt structure
41 is included as it is assumed to be negligible and can be summarised within the initial
42 measured partitioning ratio D_0 , which normalises the partition coefficient of a chosen
43 cation with a specific melt composition.

44 Amongst the few existing studies on REE partitioning with pressure, only the gar-
45 net/melt, clinopyroxene/melt and olivine/melt systems have been studied over a P -
46 range large enough to cover most terrestrial magmatic processes i.e. up to 5-6 GPa,
47 other studies being restricted to below 3.5 GPa. The garnet/melt studies show a change
48 in the P -dependence of mineral/melt partitioning, with an initially large decrease in
49 partition coefficient and a compatibility plateau after 5 GPa. (Figure 1). For Hf and Zr
50 this trend was not observed and they were largely unaffected. This would suggest that at
51 $P > 5$ GPa partition coefficients between REE and 4+ cations may become similar. The
52 transition to majorite may be the cause of this change in REEs partitioning behaviour
53 (Draper et al., 2003), however, it does so at the cost of a reduced site elasticity and
54 reduced cation size which is incompatible with mineral physics rules. To solve inconsis-
55 tencies in apparent site elasticity trends, van Westrenen and Draper (2007) introduced
56 corrections for T including an empirical correction for site elasticity by fitting a larger
57 set of garnet/melt partitioning data. Under increased T , $D^{\text{mineral/melt}}$ is expected to get
58 closer to unity due to the induced thermal disorder on crystal lattice sites. This better
59 parameterisation of the lattice strain model clearly improved its robustness, although
60 site elasticity values outside the 500-600 GPa range still cannot be reproduced. Be-
61 sides, later datasets showed the strongest P -change of $D_{\text{Lu}}^{\text{garnet/melt}}$ between 3 and 8 GPa
62 (Figure 1), where data were collected over a 100 K T -range only (Suzuki et al., 2012).
63 Datasets collected on larger P -ranges (up to 17 GPa for (Corgne et al., 2012) and 20
64 GPa for Suzuki et al. (2012) *vs* up to 10 GPa for van Westrenen and Draper (2007))
65 point out a worsening of the predictive value of the model at higher pressures. Clinopy-
66 roxene/melt partitioning studies at P up to 3.5 GPa have been parameterized by Wood
67 and Blundy (1997) and subsequent papers. The exploration of a larger compositional
68 space at 1.5 GPa demonstrated the dependence of $D_{\text{REE}}^{\text{CPx/melt}}$ on melt polymerization

69 rather than crystal composition (Gaetani, 2004), an effect restrained to compositions
70 closed to the lherzolite solidus. Higher P data collected up to 12 GPa (Suzuki et al.,
71 2012) show an overall similar P -trend to the garnet/melt system (Figure 1). In the
72 case of olivine/melt data, the REE partition coefficients decrease with increasing silica
73 in the melt at room P (Evans et al., 2008). This is at odds with the main stream of
74 studies showing the opposite behaviour (Hart and Davis, 1978; Ryerson and Hess, 1978;
75 Prowatke and Klemme, 2005; Schmidt et al., 2006), and might be taken with caution as
76 the authors pointed out the poor fit statistics (Evans et al., 2008). Under high P , REE
77 partition coefficients between olivine and peridotitic melt for 3+ cations decrease with
78 increasing pressure between 2-10 GPa (Imai et al., 2012). As for garnet, the apparent
79 site elasticity behaves anomalously with P , decreasing by 200 GPa of which the T -effect
80 can only explain a maximum of 33 GPa. Instead, Imai et al. (2012) proposed that elas-
81 ticity of the cation site in the melt affects partitioning as changes on the crystal lattice
82 alone would not produce a large enough effect. It is currently challenging to test this
83 hypothesis without a proper understanding of site elasticity in melts. It is nonetheless
84 true that the large compressibility difference between melts and crystals that exists at
85 ambient pressure largely diminishes with pressure (see Sanloup (2016) for a review and
86 references therein) as the melt becomes much harder to compress. Consequently, it
87 is expected that the strain energy resulting from the insertion of REE elements in the
88 melt ceases to be negligible. However, the fine P -mesh available for the Gt/melt system
89 implies that the strong change in P -dependence of $D_{\text{Lu}}^{\text{Gt/melt}}$ excludes a purely gradual
90 transformation, an effect that could be artificially smoothed for CPx/melt, Olivine/melt
91 systems due to the insufficient mapping of the P space. Rather, the observations on
92 garnet/melt, clinopyroxene/melt and olivine/melt systems, taken together, point to a
93 potential change in trace element local environment. As pointed out by Haigis et al.
94 (2013), if melt properties exert some control on element partitioning, their influence is
95 hidden in the adjustable parameters used in current lattice strain models, and as such,
96 cannot be predicted nor explained by the model. In their development of a predictive
97 mineral-melt partitioning model for clinopyroxene, Wood and Blundy (1997) assumed
98 that mineral-like trace element sites are present in silicate melt. However, if the nature
99 of the quasi-crystalline components changes, the energetics of partitioning are such that
100 partitioning should also change (van Westrenen et al., 2000).

101 Studies on silicate glasses, and more recently liquids, have shown that structural
102 alterations do occur within the liquid with increasing pressure. For example, major

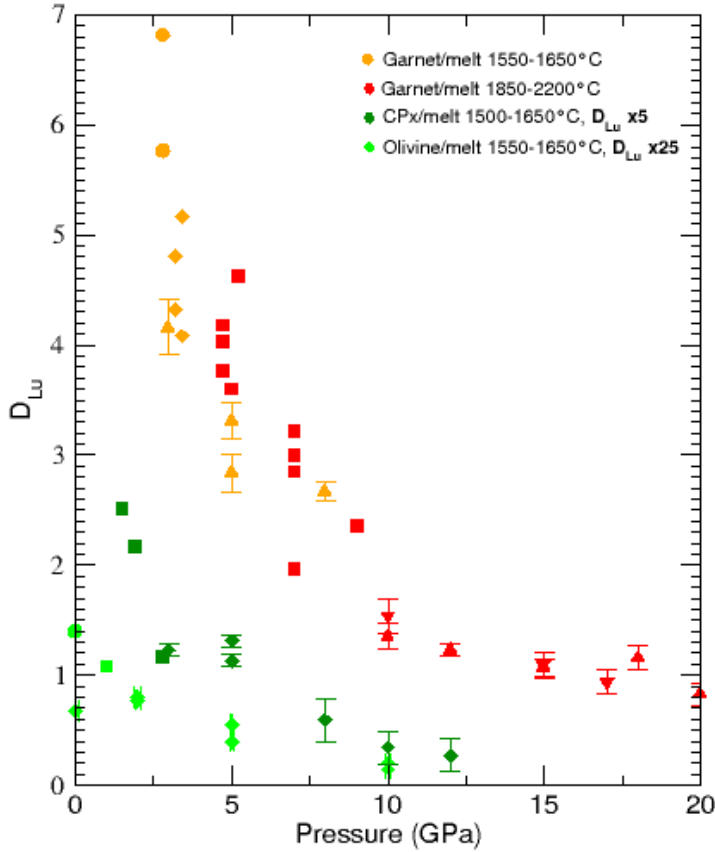


Figure 1: Mineral-melt partition coefficient data ($D_{\text{Lu}}^{\text{min/melt}}$) for Lu with pressure. For the sake of inter-comparison, $D_{\text{Lu}}^{\text{CPx/melt}}$ have been multiplied by 5, and $D_{\text{Lu}}^{\text{Olivine/melt}}$ multiplied by 25. Data presented are from studies where the composition was consistent over all P - T conditions, i.e. basaltic composition for garnet and clinopyroxene studies, and peridotitic composition for olivine studies. Other studies (i.e. van Westrenen et al. (1999)) have varying starting compositions that may mask any P effects; similarly, datasets have been limited to restricted T -range for Gt/melt and CPx/melt studies, which was not possible for olivine/melt due to the small number of studies available at high P . Symbols represent various studies; for Gt/melt (circles: Salters and Longhi (1999), diamonds: Salters et al. (2002), squares: Draper et al. (2003), up triangles: Suzuki et al. (2012), down triangles: Corgne et al. (2012)), for CPx/melt (squares: Salters and Longhi (1999), diamonds: Suzuki et al. (2012)), for Ol/melt (circle: Evans et al. (2008), squares: Salters et al. (2002), diamonds: Imai et al. (2012)). Error bars are taken from references where possible and for those not shown are smaller than the symbol size.

103 element coordination changes have been reported in silicate melts at high pressure, in-
104 cluding Si-O coordination change from 4 to 6 above 15-35 GPa (Sanloup et al., 2013;
105 Sato and Funamori, 2010) and the change in Al-O coordination from fully 4-fold co-
106 ordination to 50% 6-fold between 2-12 GPa (Drewitt et al., 2015; Yarger et al., 1995).
107 However as yet no minor element incorporation in silicate melts has been studied *in*
108 *situ* at high pressure. Simon et al. (2013) have investigated the local structural environ-
109 ment of Y in silicate glasses using Extended X-ray Absorption Fine Structure (EXAFS)
110 at ambient conditions. They studied the bonding environment of Y within the same
111 glasses as Prowatke and Klemme (2005) and discovered that increasing melt polymeri-
112 sation leads to an increase in Y coordination from 6 to 8, with a corresponding increase
113 in average bond distance from 2.28 Å to 2.38 Å. Ponader and Brown (1989) observed a
114 similar compositional variance for La with $CN_{\text{La-O}}$ increasing from 7 to 9 in the higher
115 polymerised melt, with $r_{\text{La-O}}$ also lengthening from 2.42 to 2.59 Å. In contrast, Farges
116 (1996) observed a constant CN of 6 for HFSE Zr in silicate glasses, at the exception
117 of a minor amount of octahedral Zr in their most polymerised rhyolitic composition.
118 All these studies suggest that an increase in REE coordination results in an increase in
119 bond length and indicate that important structural changes within the melt, not just
120 the crystal lattice, impact REE local structure and partitioning. Nevertheless, to date
121 all these studies have been carried out on quenched glass systems and not *in situ* at the
122 conditions of melt formation.

123 X-ray diffraction at high pressure and temperature is a well-established technique
124 for studying silicate liquid structures *in situ* (see the initial study by Funamori et al.
125 (2004) to the current highest P - T range (Sanloup et al. (2013)) but has not previously
126 been applied to trace element studies due to the low concentrations of trace elements
127 (<0.1 wt%) required to represent natural systems. X-ray diffraction has the benefit of
128 providing information on both the short and medium range structure of the melt, includ-
129 ing absolute distance and average coordination numbers, without relying on structural
130 models. In this study we employ two end member melt compositions, silicic haplogran-
131 ite and a ‘model basalt’ iron-free anorthite-diopside to monitor structural changes at
132 high pressure and temperature that may affect the incorporation of Lu at 4000 ppm
133 concentration into the melt.

Table 1: Compositions from electron microprobe analysis of both initial and recovered samples. HPG (haplogranite) and AnD (anorthite-diopside) compositions given in wt.% oxide. Analyses are based on average of a minimum of 10 sample spots, standard deviations are shown in brackets. *The low totals for the HPG composition are due to the presence of water in the sample and correspond well with the amounts added during synthesis.

| Oxide | HPG initial | HPG recovered | AnD Initial | AnD Recovered |
|--------------------------------|-------------|---------------|-------------|---------------|
| SiO ₂ | 71.6 (7) | 73.2 (4) | 48.8 (5) | 46.9 (7) |
| Al ₂ O ₃ | 10.5 (3) | 10.7 (1) | 14.7 (2) | 14.4 (4) |
| Na ₂ O | 3.3 (3) | 3.6 (2) | - | - |
| K ₂ O | 3.7 (1) | 3.8 (1) | - | - |
| MgO | - | - | 10.2 (2) | 14.2 (2) |
| CaO | - | - | 22.7 (2) | 21.6 (2) |
| Lu ₂ O ₃ | 3.9 (1) | 3.9 (1) | 3.6 (1) | 3.3 (1) |
| Totals | 93.0* (6) | 95.7* (3) | 100.2 (6) | 100.5 (6) |

134 2. Experimental Methods

135 2.1. Glass Synthesis

136 The haplogranite (HPG) and anorthite-diopside (AnD) glasses were synthesised by
137 mixing appropriate amounts of reagent grade oxides (SiO₂, Al₂O₃, MgO) and carbonates
138 (K₂CO₃, Ca₂CO₃, Na₂CO₃) from Alfa Aesar (Table 1). The corresponding degree of
139 polymerization as expressed by the NBO/T ratio is 0.4 for the HPG glass, and 1.28
140 for the AnD glass. The mixed powders were ground in an agate pestle and mortar
141 and decarbonated via a slow ramp for 12 hours at 1273 K, then fused at 1873 K in a
142 platinum crucible for 1 hour. The molten glass was quenched by immediately placing
143 the crucible into cold water. The glass was checked for homogeneity, crushed and re-
144 ground under acetone and finally fused again three times. Lu was added in the form of
145 high purity Lu₂O₃ (>99.99%) at the desired concentration (Table 1) to a portion of the
146 ground glass in order to have both a doped and plain sample of each composition for
147 comparison. This glass was crushed, re-ground, re-melted at 1873 K and re-fused three
148 times to ensure homogeneous distribution of Lu. All glasses were free from bubbles and
149 contained no signs of crystallisation. The samples were crushed to a fine homogeneous
150 powder before being loaded. The samples were free from iron to minimize the number of
151 elements with bond lengths between 2.2-2.4 Å, as these overlap the Lu-O bond distance.

152 In order to lower the melting temperature of the haplogranite to temperatures
153 achievable in a resistively heated diamond anvil cell (<1270 K), water was added to the
154 sample through high pressure addition in a piston-cylinder press. Platinum capsules
155 were welded containing finely ground haplogranite with 8-10 wt.% H₂O and held for
156 4 hours at 2 GPa and 1670 K to ensure full homogenisation. The samples were fast
157 quenched by immediately cutting power to the press. Final totals of water were between
158 6-8% over 4 runs as estimated from the recovered sample analysis (Section 2.3).

159 *2.2. X-ray Diffraction*

160 Two experimental methods were used to obtain structural data at high pressure and
161 temperature conditions. 1) Measurements on HPG melts were carried out up to 8 GPa
162 and 1100 K using angle-dispersive x-ray diffraction in resistively heated diamond anvil
163 cells (DACs) on beamline I-15 at the Diamond Light Source (Harwell Campus, UK).
164 2) Experiments on the AnD melts up to 8 GPa and 2000 K were collected on beamline
165 16-BM-B, HP-CAT, at the Advanced Photon Source (Argonne National Laboratory,
166 USA) by energy-dispersive x-ray diffraction. High P - T conditions were generated by
167 use of a Paris-Edinburgh press. Ambient temperature AnD glass data were collected
168 using DACs on beamline 13-ID-D, GSECARS, at the Advanced Photon Source by
169 angle-dispersive x-ray diffraction to ensure that the obtained structural data are not
170 dependent on the type of pressure apparatus (Figure 4 top panel). Ambient pressure
171 AnD glass data were collected on the PSICHE beamline at Synchrotron Soleil, Paris,
172 France (for Lu doped AnD glass) and at P02.2 beamline at PETRA III synchrotron in
173 Hamburg, Germany (for plain AnD glass).

174 To create the high temperature conditions in the DAC, we have used the internal
175 heating technique developed by Fei and Mao (1994) using a Pt wire. Sample was loaded
176 into the 250 μm hole of a rhenium gasket previously indented to 90 μm thickness. In
177 order to access the highest possible Q -range, we used 70° opening Boehler-Almax seats.
178 Temperature was recorded by a K-type thermocouple placed on the very edge of the
179 gasket indent as close to the sample chamber as possible. Thermocouples were previ-
180 ously calibrated using materials of known melting temperature (Pb and Na₂CO₃) in
181 order to constrain the error in temperature and the thermal gradient within the sample
182 chamber. High energy x-rays (0.2637 Å wavelength) were used to achieve maximum
183 signal intensity from the low scattering sample with a beam focussed to 70×70 μm^2 .
184 Diffraction patterns were collected for the glass and melt for 60 s using a Perkin Elmer
185 detector at each pressure point (Table 2), and a background dark image was collected

186 after each measurement in order to subtract the inherent electronic noise of the detec-
187 tor. Pressure was determined before each experiment by ruby fluorescence and at high
188 temperature it was monitored by a Pt foil inserted into the sample chamber. Diffraction
189 on the Pt calibrant was collected for 10s at each pressure before and during heating.
190 For each loading, measurements were collected on the samples, and afterwards the gas-
191 ket was unloaded and replaced in the cell in order to collect the background scattering
192 signal.

193 A detailed description of the Paris-Edinburgh press experimental techniques and cell
194 design can be found in Kono et al. (2014). The experimental conditions are detailed in
195 Table 2 with pressure determined from the cell-volume change of the pressure transmit-
196 ting medium in the form of an MgO cylinder. Temperature was estimated by previous
197 power calibrations using this cell assembly (Kono et al. (2014)). This calibration also
198 accounts for the effect on pressure of the distance between the sample and MgO ring at
199 high temperature using the P - V - T relation of MgO and elastic wave velocity measure-
200 ments (Kono et al. (2010)). Diffraction patterns on the MgO were collected at room
201 temperature and above the melting temperature. X-ray diffraction was collected for
202 2 hours using an energy-dispersive germanium solid-state detector at ten 2θ angles (2° ,
203 2.7° , 3.5° , 5° , 7° , 10° , 15° , 20° , 27° , 35°) enabling coverage up to 20 \AA^{-1} in reciprocal
204 space with $Q = 4\pi E \sin \theta / 12.398$, where E is the energy of the x-rays in keV up to
205 >100 keV.

206 *2.3. Recovered Sample Analysis*

207 Recovered HPG quenched samples were polished for electron microprobe analysis
208 at the EMMAC (The Edinburgh Materials and Micro-Analysis Centre), University of
209 Edinburgh. Analyses were carried out using a CAMECA SX100 electron microprobe
210 with an accelerating voltage of 15 keV and $8 \mu\text{m}$ beam size. Where glass was recovered
211 the samples retained a stoichiometry nearly identical to their starting compositions
212 (Table 1); therefore it is unlikely the samples underwent any major chemical change
213 during the experiments and no loss of Lu. Back scattered electron images taken of
214 the sample show no evidence for quench crystallisation and the sample appears glassy
215 (Figure 2b). Bubbles are present in the HPG which is probably due to exsolution
216 of water during quenching indicating that water remained in the sample during the
217 experiment. The low microprobe totals (Table 1) for the HPG composition are due
218 to the presence of water in the sample. Quenched AnD samples were analysed at the
219 Centre de Microanalyse Camparis, University Pierre and Marie Curie. These results

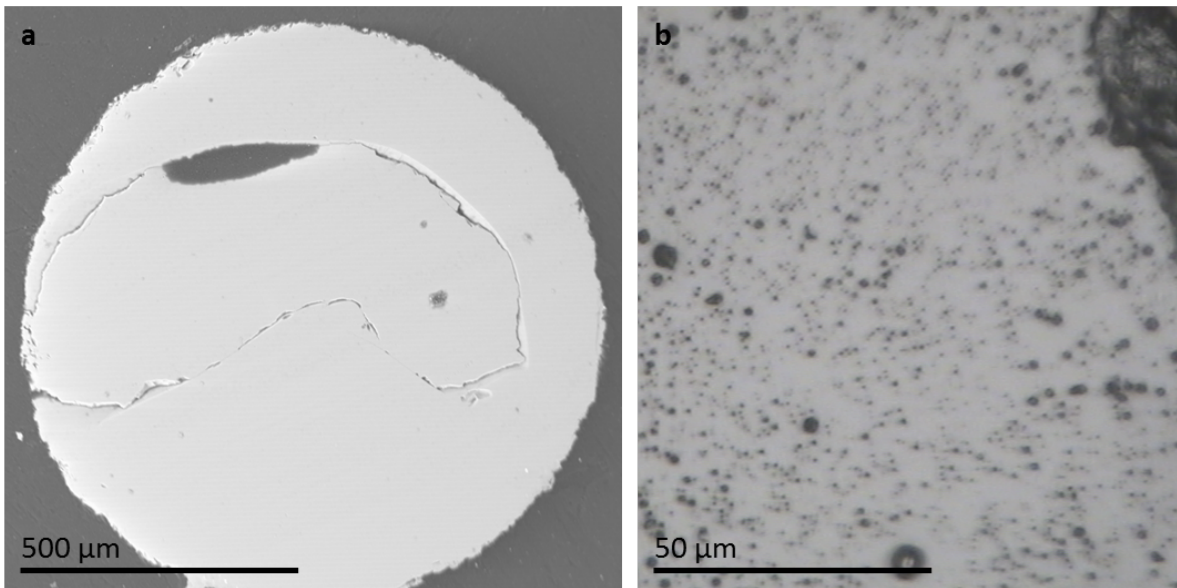


Figure 2: Left: Recovered sample from AnD experiment A8-a using a Paris-Edinburgh press. Right: Recovered sample from HPG experiment D8 from resistive heated DAC polished within Re gasket. Spots are bubbles within the hydrous sample.

220 (Table 1) show that when the sample quenched to a glass (Figure 2a) the composition
 221 after the experiment was nearly identical.

222 2.4. Data Processing

223 Angle-dispersive diffraction patterns were radially integrated using FIT2D (Ham-
 224 mersley (1996)), with a mask applied to crystalline Bragg peaks that arise from diffrac-
 225 tion of the single crystal diamond anvils. The measured experimental intensity, $I(Q)$,
 226 contains scattering by both the sample and background contributions, where $Q =$
 227 $\frac{4\pi}{\lambda} \sin \theta$ and λ is the x-ray beam wavelength. In order to isolate the intensity that con-
 228 tains only the structural information, corrections for background intensity, $I_B(Q)$, and
 229 attenuation, $A(Q)$, from the sample must be made to the measured intensity given by

$$I(Q) = I_s(Q) + A(Q)I_B(Q) + I_{inc}(Q), \quad (1)$$

230 where $I_s(Q)$ represents the scattering from the sample containing only structural
 231 information, and $I_{inc}(Q)$ represents the incoherent scattering from the atoms, arising
 232 from the sum of the self $\sum_{\alpha} c_{\alpha} f_{\alpha}(Q)^2$ and Compton scattering $\sum_{\alpha} c_{\alpha} C_{\alpha}(Q)$, where
 233 c_{α} is the concentration of species α . The values for the self and Compton scattering

234 amplitudes are documented by Hajdu (1972); Hubbell et al. (1975). The Faber-Ziman
 235 total structure factor, $S(Q)$, (Faber and Ziman (1965)) is then determined by;

$$S(Q) - 1 = \frac{K[I_s(Q) - A(Q)I_B(Q)] - I_{inc}(Q)}{\langle f^2(Q) \rangle}, \quad (2)$$

236 where K is required to normalise the data to the incoherent scattering profile and the
 237 total structure factor is normalised to the average scattering $\langle f^2(Q) \rangle = (\sum_{\alpha} c_{\alpha} f_{\alpha}(Q))^2$.
 238 The radial distribution functions, $G(r)$, are then obtained from a Fourier transform of
 239 the $S(Q)$ as:

$$G(r) - 1 = \frac{1}{2\pi^2 r n_0} \int_0^{\infty} Q[S(Q) - 1] \sin(Qr) dQ, \quad (3)$$

240 where n_0 is the atomic density in atoms per \AA^3 and the experimental values are listed
 241 in Table 2. The densities were estimated by fixing $CN_{\text{Si-O}} = 4$ and $d_{\text{Si-O}} = 1.61 \text{\AA}$ and
 242 integrating under the Si-O contribution for each run (cf section 3.2 and Table 2), as
 243 well as applying self-consistency checks. These included ensuring the $S(Q)$ followed the
 244 sum rule $\int_0^{\infty} [S(Q) - 1] Q^2 dQ = -2\pi n_0$, and that at low- r any unphysical oscillations
 245 were minimised as $G(r = 0) = 0$ (Zeidler et al. (2009); Drewitt et al. (2013)).

246 For the energy dispersive x-ray diffraction data collected on HP-CAT, Bragg peaks
 247 arising from the diffraction of graphite in the cell assembly, and fluorescence of indium
 248 on the detector and Lu were removed at each angle. If peaks were at $>30\%$ concentra-
 249 tion between the energies of interest (25 to 55 keV) the data were discarded. Where
 250 required, fits were made to the data to extrapolate the signal after the Bragg peaks were
 251 removed. The aEDXD program developed by Changyong Park (see Kono et al. (2014))
 252 was then used to scale the primary beam by least squares fitting at the highest 2θ angle,
 253 and an evenly spaced $S(Q)$ function was produced by error weighted spline smoothing
 254 of the merged data in Q -space. This technique is based on the highest diffraction angle
 255 oscillating around 1 because as $Q \rightarrow \infty$, $S(Q) \rightarrow 1$. The $G(r)$ was then obtained by
 256 Fourier Transform of the spline smoothed $S(Q)$ (Equation 3).

257 For the sake of comparison between EDX and ADX data, all $S(Q)$ were cut at
 258 12\AA^{-1} in order to have the same spatial resolution in the direct space on obtained
 259 $G(r)$.

Table 2: P - T conditions of each experimental run as well as estimated densities and results on positions of the first two peaks in the $G(r)$, r_{1-2} . Errors for P and T shown in brackets. Experiment 1 on HPG was carried out on I-15 at the Diamond Light Source. Where both glass and high T data were collected, the density in [] is from the melt. Peak positions are shown only for high T phases unless none were collected. * on temperature indicates where the thermocouple failed during the run and a minimum T was estimated from recrystallisation of Pt and previous thermocouple calibrations. Experiment 2: Collected on HP-CAT at the Argonne Photon Source in June 2014 (-a) and February 2016 (-b). ! represents where the 2nd peak arises from the O-O contribution producing a shoulder on the r_3 peak. † denotes collection at synchrotron Soleil, PSICHE. ‡ denotes collection at Petra P.02 DESY.

| Run no. | Comp. | P (GPa) | T (K) | n_0 (\AA^{-3}) | $G(r)$ positions (\AA) | |
|---------|--------------|-----------|-----------|-----------------------------|-----------------------------------|--------|
| Exp. 1 | | | | | r_1 | r_2 |
| D1 | HPG | 1.4 (2) | 290 | 0.07 | 1.6 | - |
| D2 | HPG | 2.3 (3) | 920 (50) | 0.075 [0.067] | 1.6 | - |
| D3 | HPG | 4.1 (3) | 390 | 0.077 | 1.62 | - |
| D4 | HPG + Lu | 0.5 (2) | 910* (50) | 0.069 [0.066] | 1.59 | 2.33 |
| D5 | HPG + Lu | 2.1 (3) | 900* (50) | [0.071] | 1.6 | 2.37 |
| D6 | HPG + Lu | 2.5 (3) | 290 | 0.073 | 1.59 | 2.36 |
| D7 | HPG + Lu | 3.8 (2) | 973 (40) | 0.079 [0.078] | 1.6 | 2.36 |
| D8 | HPG + Lu | 5.8 (4) | 1073 (40) | 0.083 [0.082] | 1.59 | 2.35 |
| Exp. 2 | | | | | | |
| Amb1 | AnD (†) | 0 | 290 | 0.081 | 1.62 | 2.41 |
| Amb2 | AnD + Lu (‡) | 0 | 290 | 0.081 | 1.62 | 2.36 |
| A1-b | AnD | 0.8 (3) | 1570 (50) | 0.082 | 1.59 | 2.78 ! |
| A2-b | AnD | 2.4 (2) | 1670 (50) | 0.084 | 1.61 | 2.76 ! |
| A3-b | AnD | 3.5 (3) | 1720 (50) | 0.087 | 1.59 | 2.76 ! |
| A4-b | AnD | 4.8 (3) | 1770 (50) | 0.09 | 1.59 | - |
| A5-b | AnD | 6.5 (3) | 1870 (50) | 0.092 | 1.60 | - |
| A6-b | AnD | 8.0 (4) | 2070 (60) | 0.092 | 1.61 | - |
| A7-b | AnD + Lu | 0.8 (3) | 1570 (50) | 0.082 | 1.59 | 2.34 |
| A8-a | AnD + Lu | 2.1 (3) | 2020 (80) | 0.084 | 1.61 | 2.34 |
| A9-b | AnD + Lu | 3.1 (3) | 1570 (50) | 0.09 | 1.59 | 2.32 |
| A10-b | AnD + Lu | 4.2 (3) | 1750 (50) | 0.091 | 1.62 | 2.32 |
| A11-a | AnD + Lu | 5.2 (3) | 1850 (50) | 0.094 | 1.62 | 2.41 |
| A12-b | AnD + Lu | 7.0 (3) | 2120 (50) | 0.093 | 1.61 | 2.43 |

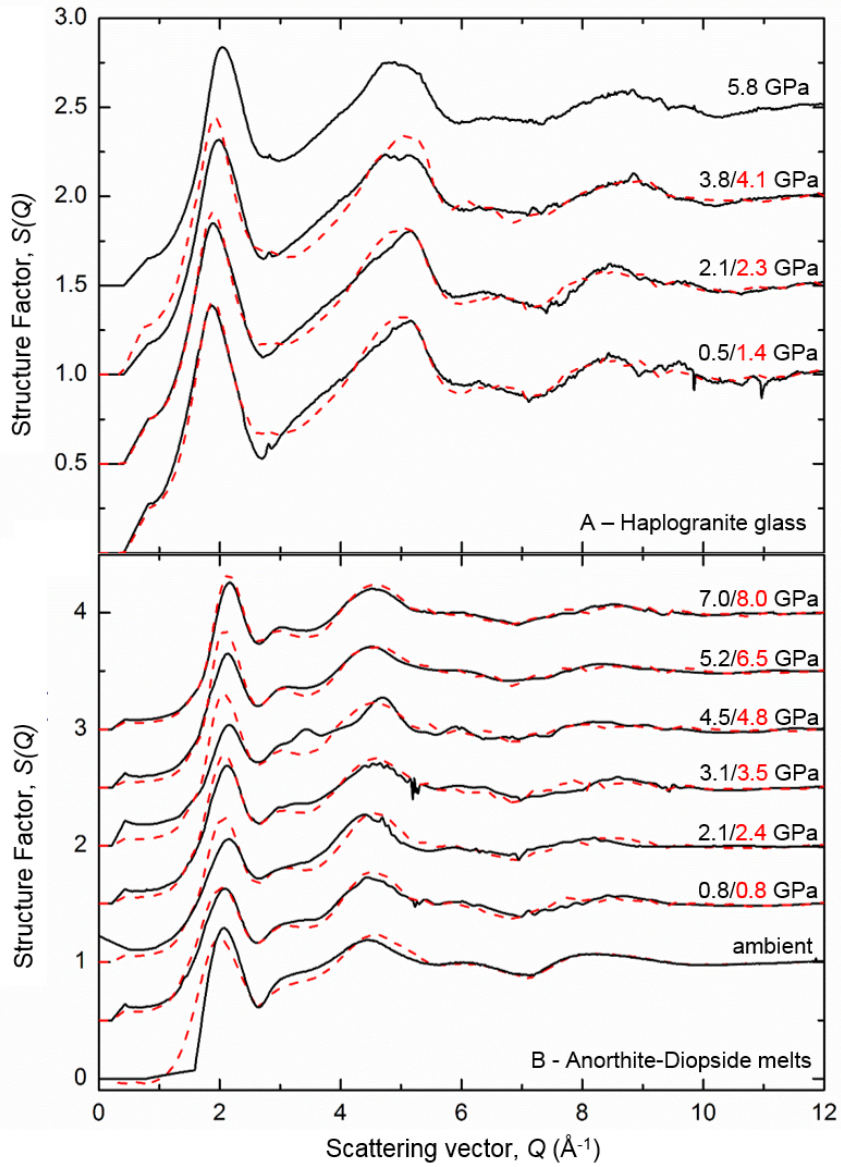


Figure 3: $S(Q)$ for samples listed in Table 2. Black solid lines show Lu doped samples and red dashed curves are the undoped samples at similar pressures. Top panel (A) shows HPG data with pressures shown for the Lu-doped measurements, and undoped glass spectra within 0.5 GPa of these. Glass measurements are shown due to a lack of high- T data at each P , however as discussed in Section 3.1, the HPG glass is analogous to the melt. Lower Panel (B) shows AnD melt experiments at >1500 K and undoped samples are within 1 GPa of given P .

260 3. Results

261 3.1. Overall structural description

262 Ambient and high temperature data were collected on Lu-doped and undoped sam-
263 ples at similar pressure points and when possible, quench measurements were taken on
264 all runs (Table 2). The $S(Q)$ and $G(r)$ are shown in Figures 3 and 4. During heating
265 HPG samples, at temperatures >850 K the samples either recrystallised or remained
266 amorphous due to the strong glass forming nature of SiO_2 -rich liquids. On these time
267 scales (>1 hour) recrystallization would be expected to occur above the glass transi-
268 tion temperature at ~ 850 K (Dingwell, 1998). Therefore, if recrystallization did not
269 occur at these temperatures, the samples were in the super-cooled liquid state. Two
270 experiments (D2 and D7) were conducted at T exceeding the liquidus temperature for
271 haplogranite (Holtz et al. (1992)). From our results, the local environment of Lu in the
272 melt phase and the ambient temperature glass phase are identical as no changes were
273 observed in the corresponding $G(r)$ (grey and red solid lines on Figure 4). In Figure
274 3A the first sharp diffraction peak (FSDP) is seen at 1.98 \AA^{-1} at 0.5 GPa-room T with
275 little change over the P -range presented here (up to 2.01 \AA^{-1} at 5.8 GPa-room T). This
276 is higher than in the dry HPG glass where the FSDP is at 1.67 \AA^{-1} and reflects the
277 depolymerisation of the glass induced by water (Anderson et al., 2014), an effect also
278 reported by forsterite-enstatite melts (Yamada et al., 2007). Alteration to the $S(Q)$
279 from the scattering of Lu is seen in the 2nd peak between $3\text{-}5 \text{ \AA}^{-1}$, where the peak
280 appears less broad in the Lu-doped case with slightly greater intensity on the upward
281 slope at $3\text{-}4 \text{ \AA}^{-1}$.

282 The measured $S(Q)$ for the Lu doped AnD compositions are shown in the lower
283 panel (B) of Figure 3 along with undoped samples for comparison. The FSDP shows a
284 gradual increase from 2.05 to 2.1 \AA^{-1} from ambient conditions to 7 GPa. An increase in
285 the FSDP has been seen for other silicate glass and melt compositions and is attributed
286 to the collapse of open cages in the SiO_2 network (Benmore et al. (2010); Meade et al.
287 (1992)). A similar increase in intensity between $3\text{-}4 \text{ \AA}^{-1}$, as observed in the HPG, is
288 seen in the Lu-doped AnD $S(Q)$.

289 The resulting real space distribution functions, $G(r)$, are shown in Figure 4B. The
290 main peak positions, atomic densities and uncertainties in real space for each data
291 point are detailed in Table 2. In both compositions the first peak in the $G(r)$, r_1 , is
292 attributed to the $d_{\text{Si-O}}$ at $1.61(2) \text{ \AA}$ with 4-fold coordination as shown in other silicate
293 glass, liquid and crystalline structures (Sato and Funamori (2010); Meade et al. (1992)).

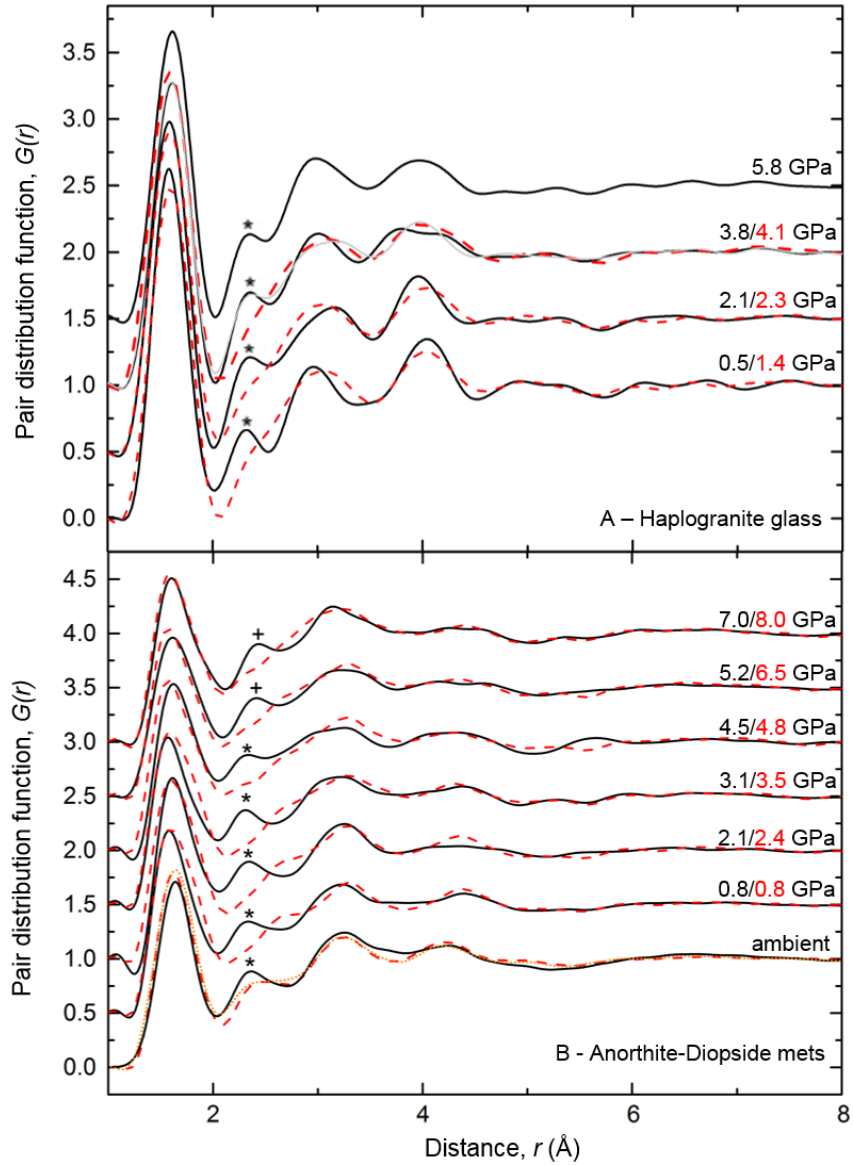


Figure 4: Radial distribution functions from the $S(Q)$ shown in Figure 3 and detailed in Table 2. Black solid lines are Lu-doped and red dashed are undoped samples as described in Figure 3. In the HPG (A) grey solid line was collected at high- T and show the similarity between molten high P HPG samples and their respective glass. * highlights the effect of Lu-O on the $G(r)$ and r_2 position. In the AnD (B), at >5 GPa, the + marks where the peak shifts to higher r . In the AnD (B) dotted orange line was collected using a DAC at room T and is similar to the $G(r)$ obtained using a PE cell.

294 In the HPG, the second peak, r_2 , only appears within the doped samples (D4-D8) at
 295 2.36 (3) Å and is attributed to the Lu-O bond distance. In the undoped AnD, the
 296 second contribution arises from the Ca-O correlations at ~ 2.4 Å and overlaps the Lu-
 297 O distance. However the r_2 peak in the doped AnD can be clearly seen to increase
 298 in intensity and shift to lower r with the introduction of Lu in the ambient samples
 299 (Figure 4B). The correlations observed at 3.0(2) Å in the HPG and 3.2(3) Å in the
 300 AnD are attributed to the sum of the O-O and Si-Si contributions and match well with
 301 $G(r)$ observed in other studies (Crépeisson et al. (2014); Sanloup et al. (2013)) and with
 302 MD simulations by Vuilleumier et al. (2009) on similar compositions. In the HPG,
 303 this correlation sharpens in the presence of Lu, potentially reflecting increased ordering
 304 of the Si-Si distribution, an effect not observed for the AnD melts within the noise
 305 level. In the HPG a fourth correlation is visible at 4 Å, this can be attributed to the
 306 2nd interaction of Si-O and is much more pronounced in the HPG due to the higher
 307 concentration of SiO₂.

308 3.2. Fit of the Lu-O contribution

309 The radial distribution function $G(r)$ is the sum of all the individual ion-ion inter-
 310 actions within the sample, where each individual Gaussian, $g(r)_{\text{ind}}$, represents a single
 311 ion-ion contribution. This was fit using the following relations:

$$G(r) = \sum g(r)_{\text{ind}} = \frac{1}{n_0 S_\infty} \sum_i \frac{x_i A_i}{\sigma_i \sqrt{2\pi}} \exp\left(-\frac{(r - d_i)^2}{2\sigma_i^2}\right), \quad (4)$$

312 where;

$$A_i = \frac{CN_i}{\int \frac{4\pi r^2}{\sigma_i \sqrt{2\pi}} \exp\left(-\frac{(r-d_i)^2}{2\sigma_i^2}\right) dr}. \quad (5)$$

313 The coordination number for the individual ion-ion contributions, CN_i , is related
 314 to the integral under each individual Gaussian by the density, n_0 , and concentration,
 315 x_i , of the species. The interatomic distance is d_i and $\sigma_i = k\sqrt{d_i}$ defines the width of the
 316 Gaussian using an adjustable parameter k (Hosemann and Bagchi (1962)), with values
 317 ranging from 0.07 to 0.2 depending on the ion-ion contribution. Over this pressure and
 318 temperature range it is assumed that the Si-O coordination, $CN_{\text{Si-O}}$, of 4 and bond
 319 length, $r_{\text{Si-O}}$, of 1.61 Å remain unchanged (Benmore et al. (2010); Sanloup et al. (2013);
 320 Sato and Funamori (2010)). Other known peak positions, i.e. Al-O for HPG and Al-O,
 321 Mg-O and Ca-O for AnD, and coordination numbers are taken from literature (Guillot

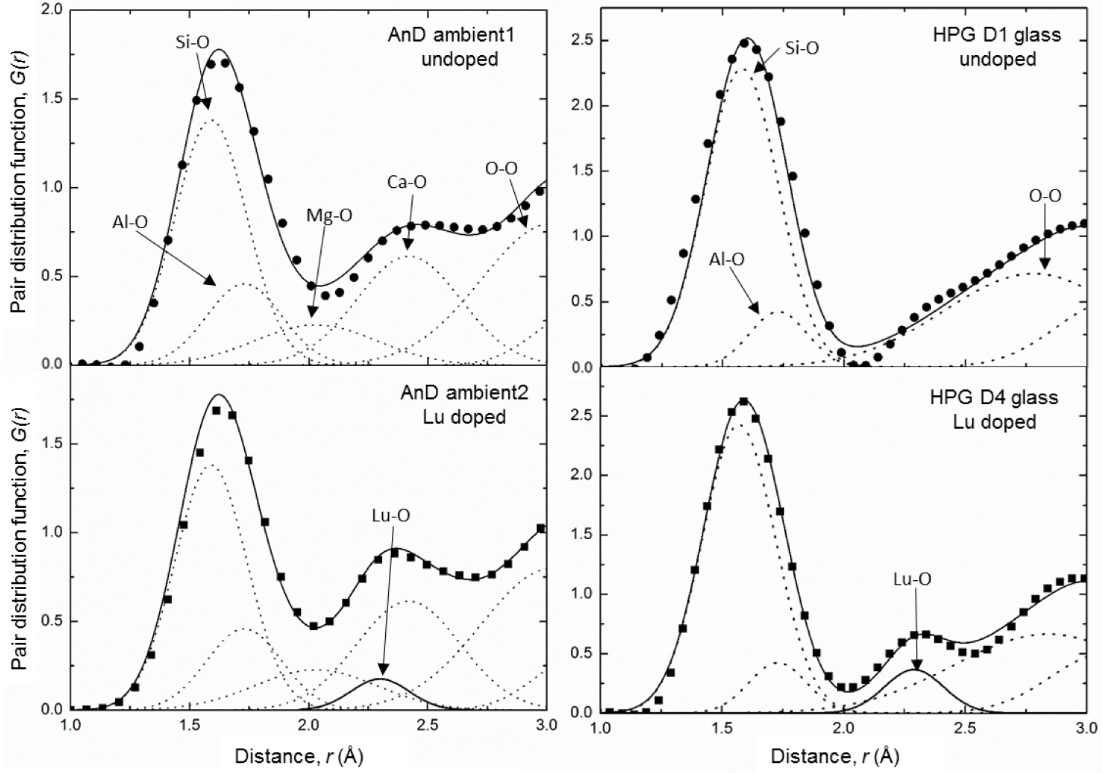


Figure 5: Measured $G(r)$ (black markers) from Figure 4 shown with Gaussian fits to both the plain (upper panels) and doped (lower panels) samples. Individual Gaussians, $g_{\text{ind}}(r)$, for ion-ion contributions are labelled (dotted lines) along with the total sum of Gaussians (solid black line). Left panels show the AnD compositions and right panels, the HPG. Lu-O contributions are shown in the doped figures by a thick black line and are labelled as Lu-O. Major element fit parameters are identical between the doped and undoped samples using parameters described in Table 3.

Table 3: Ion-ion contributions used to model individual Gaussians, $g(r)_{\text{ind}}$ for both compositions. * indicates values taken from references cited in the text, all others are fitted. The coordination numbers obtained for Lu are an average over a minimum of 10 fits with error of ± 0.3 for each final value. d_i = bond length, CN_i = coordination of individual bond. ‘-’ indicates that the value is identical to above mentioned.

| <i>P</i> -independent contributions | | | | | | | | | |
|-------------------------------------|----------|--------|----------|----------|---------|----------|----------|----------|--------|
| HPG | | | | | AnD | | | | |
| Si-O | | | Lu-O | | Si-O | | Mg-O | | |
| d_i | CN_i | | d_i | CN_i | d_i | CN_i | d_i | CN_i | |
| 1.6 (2) | 4* | | 2.36 (3) | 8.1 | 1.6 (2) | 4* | 2.00 (5) | 5* | |
| <i>P</i> -dependent contributions | | | | | | | | | |
| HPG | | | AnD | | | | | | |
| P | Al-O | | P | Al-O | | Ca-O | | Lu-O | |
| (GPa) | d_i | CN_i | (GPa) | d_i | CN_i | d_i | CN_i | d_i | CN_i |
| 0.5 | 1.73 (1) | 4.1* | 0.8 | 1.73 (1) | 4.3* | 2.40 (2) | 7* | 2.29 (2) | 6.2 |
| 2.1 | - | 4.1* | 2.1 | - | 4.5* | - | 7.2* | 2.32 (2) | - |
| 2.5 | - | 4.2* | 3.1 | - | 4.5* | - | 7.4* | 2.30 (2) | - |
| 3.8 | - | 4.4* | 4.5 | - | 4.6* | - | 7.6* | 2.32 (2) | - |
| 5.8 | - | 4.6* | 5.2 | - | 4.7* | - | 8.2* | 2.39 (2) | 7.9 |
| | | | 7.8 | - | 4.9* | - | 8.3* | 2.41 (2) | - |

322 and Sator (2007a,b); Sun et al. (2011); Drewitt et al. (2015), and listed in Table 3). Na
323 contribution is insignificant to the total $G(r)$ due to its light scattering so is not shown
324 here, as in rhyolitic $G(r)$ models by Vuilleumier et al. (2009). Bond distances above
325 3 Å (e.g. K-O, Si-Si) do not contribute to the signal below the Lu-O contribution and
326 were fitted as a single contribution.

327 Initially the undoped data for each pressure are fitted with a sum of Gaussians to
328 obtain interatomic distances for major element ion-ion contributions at $r < 2.5$ Å along
329 with the O-O contribution (Figure 5), and the same parameters are used to fit the Lu-
330 doped data. This results in the isolation of the fit parameters required for $CN_{\text{Lu-O}}$ and
331 $d_{\text{Lu-O}}$ (Table 3 and Figure 5). This technique limits the uncertainty that arises from
332 fitting complex pair distribution functions but errors in the average coordination arise
333 from the asymmetry of the real $g(r)_{\text{ind}}$ correlations and their high r oscillations.

334 3.3. Lutetium incorporation

335 In the HPG melt, a bond distance $r_{\text{Lu-O}} = 2.36(3) \text{ \AA}$ was observed and found to be
336 invariable with pressure within the accuracy of this technique. The average $CN_{\text{Lu-O}}$
337 was determined to be 8.1(3) at all pressure and temperature conditions. For the AnD
338 a $CN_{\text{Lu-O}}$ of 6.2 (3) and a $r_{\text{Lu-O}}$ of 2.29 (2) \AA were determined for the lowest pressure
339 data ($<5 \text{ GPa}$) and the ambient doped glass. The higher pressure points show a clear
340 shift in fit correlation to a higher $r_{\text{Lu-O}}$ of 2.40 (3) \AA and an estimated $CN_{\text{Lu-O}}$ of 7.9
341 (3) (Table 3, Figure 6). This change appears to be abrupt, occurring within 1 GPa
342 (from the accuracy of our data points), and it only affects the Lu-O contribution. This
343 is unlike major element coordination changes which undergo a transition over a broad
344 pressure range (Sato and Funamori (2010); Drewitt et al. (2015); Yarger et al. (1995)).
345 At two pressure points data were also collected at three temperatures over a 400 K
346 range (Supplementary Material). The Lu-O contribution in AnD seems unaffected by
347 T at least within the uncertainties of the method, i.e. 0.2 \AA on bond length and 0.2 on
348 the coordination number.

349 Crystalline oxide bond lengths for Lu-O are in good agreement with the distance of
350 the r_2 correlation at ambient pressure. Six-fold coordinated Lu-O in oxides is reported
351 to be 2.24 \AA and 8-fold coordinated Lu-O at 2.32 \AA which agree with tabulated ionic
352 radii by Shannon (1976). Studies on other REE glasses, e.g. YbSiAlO/N, have found
353 similar parameters with Yb-O coordination at 6 and a bond length of 2.22 \AA (Uhlig
354 et al. (1998)). Other REE-O such as Dy and La in sodium silicates show decreasing
355 bond length with atomic radii due to the lanthanide contraction, with 6-fold Dy-O at
356 2.29 \AA and La-O at 2.48 \AA . In this study, a coordination $CN_{\text{Lu-O}}$ of 6 gives rise to a
357 bond distance of 2.29 \AA , and $CN_{\text{Lu-O}}$ of 8 gives 2.36-2.4 \AA , as might be expected in the
358 liquid this distance is slightly longer than those of the solids.

359 4. Discussion

360 To our knowledge this is the first experimental study of its kind to identify the
361 structural incorporation of trace elements *in situ* within a silicate melt structure at
362 high pressure, previous EXAFS data having been measured on glasses at ambient con-
363 ditions. As the ambient pressure results presented for $CN_{\text{Lu-O}}$ in glasses corroborate
364 coordinations and bond lengths of Y, a geochemical proxy for Lu but with a lower
365 absorption K-edge energy that makes it suitable for EXAFS analysis (Simon et al.,
366 2013), this method appears to provide a reliable tool for determining REE speciation

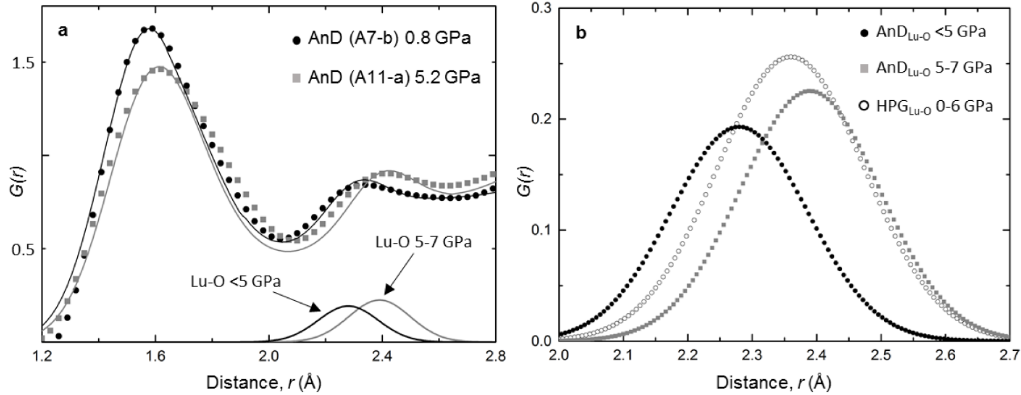


Figure 6: a) Change in fits for Lu-O in AnD with P increase above 5 GPa. $G(r)$ for a low P AnD melt (black circles) and high P AnD melt above the Lu-O coordination change (grey squares) and their respective fits (solid lines) are shown. Individual $g(r)_{\text{Lu-O}}$ are marked with a clear shift to higher r seen above 5 GPa. b) Individual $g(r)_{\text{Lu-O}}$ for low P AnD (black circles), high P AnD (grey squares) and average for HPG (high silica) over the P range studied (open circles).

367 within silicate melts. A major consideration for this technique is that it is reliant on
 368 the applicability of Henry’s law as in order to use trace elements in models it is as-
 369 sumed that the activity, and hence partitioning of trace elements, is independant of
 370 concentration below a given limit. This is because at such low concentrations they
 371 form an insignificant structural part of a phase and do not alter the thermodynamics
 372 of the system. Although Lu here is not at natural levels of concentration (<2 ppm),
 373 in this system we propose that Henry’s law is still obeyed as: 1) At concentrations of
 374 4000 ppm Lu ions are highly unlikely to interact with each other. 2) Many studies
 375 on partitioning of trace elements have shown that Henry’s law is still obeyed even at
 376 several wt. % concentration of trace elements (Beattie (1993); Prowatke and Klemme
 377 (2006)). 3) There is a close similarity here with other results on REE (La, Gd and Yb)
 378 at much lower concentrations (Ponader and Brown, 1989).

379 4.1. Compositional effect

380 At low pressure, <5 GPa, the results presented show an increase in Lu coordination
 381 from 6 to 8 with increasing silica content of the melt, from AnD to HPG, coincident
 382 with an increase in bond length of 0.07 (3) Å (Figure 6b). This is consistent with ob-
 383 servations on Y-O in silicate and aluminosilicate glasses at ambient conditions (Simon
 384 et al. (2013)), and MD calculations on Y-O in aluminosilicate melts (Haigis et al., 2013).

385 As discussed in the introduction, this compositional effect is attributed to the higher
386 availability of non-bridging oxygens in the basaltic network due to the presence of oxy-
387 gens weakly bonded to Ca atoms (Haigis et al., 2013). This is reflected in the narrower
388 distribution around a shorter mean Lu-O distance calculated for less polymerised melts
389 (Haigis et al., 2013) and observed in the present work (Figure 6b and width parameters
390 reported in Table 3). The results for the HPG presented here are all for a hydrous com-
391 position. We measure the same Lu-O coordination number in our hydrous composition
392 than reported in dry silicate glasses for Y (Simon et al., 2013). This indicates that
393 the absence of water would not affect our results. Since water de-polymerises the melt
394 structure (Mysen et al., 1980) as can be seen by the shift of the first sharp diffraction
395 peak to high Q -values initially reported for hydrous forsterite-enstatite melts (Yamada
396 et al., 2007) and observed here as well (cf section 3.1), this in turn implies that Lu does
397 not enter the ring structure as expected from its large size.

398 4.2. Pressure effect

399 Within the HPG there is no observable pressure effect on Lu incorporation within
400 the melt structure up to 8 GPa. Silica rich melts are predominantly comprised of
401 interconnected rings of tetrahedra that form cages (Kohara et al., 2011). As pressure
402 increases these collapse as the network is compressed and reaches a packing limit around
403 5 GPa (Wang et al., 2014). However as Lu is unlikely to be accommodated within the
404 cages there is little compressional effect on its speciation within the melt. Within the
405 AnD, however, an increase in P causes an abrupt coordination increase between 4-
406 5 GPa, accompanied by an increase in the bond length from 2.29 to 2.40 Å (Figure 6).
407 Therefore above 5 GPa the CN_{Lu-O} and r_{Lu-O} are similar to that of the HPG. At high
408 pressures, as the packing limit of the melt is reached, Lu is forced onto ‘crystal-like’
409 sites and coordination increases. The presence of these ‘crystal-like’ sites in the melt
410 was suggested by van Westrenen et al. (2000), who suggested that oxide like, J_2O_3 , and
411 garnet like, $J_3Al_5O_{12}$, sites might exist in the melt structure and influence partition
412 coefficients due to the site elasticity and radii. van Westrenen et al. (2000) showed that
413 partitioning behaviour between silicate melt and garnets could be better explained by
414 the presence of $J_3Al_5O_{12}$ sites with 8-fold coordination within the melt, rather than 6-
415 fold J_2O_3 sites. As pressure increases and the melt is packed more closely together it is
416 likely that more ‘crystal-like’ sites are created within the melt with a higher coordination
417 environment. These have a similar bonding environment to sites within minerals such as
418 garnet and therefore a reduction at high P in partition coefficient between the melt and

419 minerals, where REE³⁺ are usually compatible, would be expected. It is also interesting
420 to note that Ca atoms, that constitute the second shell of neighbours around Lu after
421 O atoms in depolymerised melts (Haigis et al., 2013), get progressively bonded to more
422 O atoms in the 0-10 GPa interval with a Ca-O coordination number increasing from 7
423 to 9 (Guillot and Sator, 2007a; Sun et al., 2011; Drewitt et al., 2015).

424 4.3. Impact on Partition Coefficients

425 The coordination change from 6 to 8 as melt polymerisation increases (i.e. from
426 the AnD to the HPG) corresponds with results presented by Prowatke and Klemme
427 (2005) and Schmidt et al. (2006) on the dramatic increase in REE partition coefficients
428 with melt polymerisation. This increase in compatibility and preference to incorporate
429 in the mineral as polymerisation of the melt increases has been proposed to be due
430 to the energetics associated with bonding to predominantly bridging oxygens. In de-
431 polymerised melts the large sites and freely available non-bridging oxygens mean that
432 at lower P the REEs can more easily incorporate into the melt structure than in the
433 crystal lattice. Although we find that Lu has the same coordination in polymerised
434 melts as the basaltic melts at >5 GPa, existing partitioning studies would suggest that
435 the site or mechanism for Lu incorporation in these melts is different as opposite par-
436 titioning behaviour is observed (between low pressure basaltic and granitic melts an
437 increase in D_{Lu} is witnessed, but a decrease in D_{Lu} between low pressure and >5 GPa
438 basaltic melts).

439 From these results we propose that in basaltic systems, the melt has a much stronger
440 influence on $D^{\text{min/melt}}$ with pressure than previously expected. The observed decrease
441 in compatibility with P (Figure 1) could occur in relation with the observed change of
442 local structural environment of Lu in the melt. The coordination change in the melt
443 at 5 GPa results in the plateauing of the $D_{\text{REE}}^{\text{min/melt}}$ as there is little preference for either
444 the mineral or melt at this pressure. This change of local structural environment most
445 likely implies a variation of the volume change of the partitioning reaction between
446 mineral and melt. This is consistent with the previous findings from Corgne et al.
447 (2012) who attributed the factor of 2 mismatch between their measured $D_{\text{REE}}^{\text{garnet/melt}}$ and
448 those predicted by the van Westrenen&Draper (2007) model to the P -dependence of
449 the reaction volume change that is not accounted for.

450 In other words, the change of local environment of Lu in melts implies that both the
451 pre-exponential term, D_0 , and site elasticity terms be revised in the lattice strain models
452 to explicitly model not only the crystal part but also the melt contribution to element

453 partitioning. Structural changes in the melts have been advocated to explain the abrupt
454 changes in the P -dependence of $D^{\text{magma/metal}}$ for Ni, Co, W circa 5 GPa (Kegler et al.,
455 2008; Cottrell et al., 2009; Keppler and Rubie, 1993; Sanloup et al., 2011) and 35 GPa
456 (Sanloup, 2016). The observed change of P -dependence of $D^{\text{magma/metal}}$ for Ni, Co,
457 W, of $D_{\text{Lu}}^{\text{mineral/melt}}$ for garnet, clinopyroxene and olivine/melt systems above 5 GPa
458 can either be a mere coincidence, or suggest instead an important structural control
459 from the silicate melt. The comparison of molten basalt density with crystalline basalt
460 (i.e. eclogite) density shows that the large crystal-melt density difference at room P
461 is divided by 3 at 5 GPa, and almost vanishes above 50 GPa (Sanloup, 2016). The
462 structural control of magmas on element partitioning may thus occur through both
463 abrupt changes of coordination number as reported here for Lu, and through large
464 changes of melt compressibility.

465 5. Conclusions

466 This study shows that x-ray diffraction techniques can be used to study trace ele-
467 ment incorporation in liquids at high pressure and can reliably determine the nearest-
468 neighbour bond distances for minor elements. Our results show an increase in coordi-
469 nation from 6 to 8 of Lu with increasing polymerisation of the melt, consistent with
470 an increase in the $D^{\text{mineral/melt}}$ partitioning ratio from <1 to >100 . These results are
471 consistent with other studies carried out on Y, Zr, Th and La with changing glass
472 polymerisation. This data suggest that the coordination of REE in highly polymerised
473 compositions is similar in the glass and melt and also remains constant up to 6 GPa.

474 An abrupt coordination increase from 6 to 8 is observed at 4-5 GPa in less poly-
475 merised systems. This coordination change suggests that at >5 GPa compression of
476 the melt results in the formation of ‘crystal like’ sites that accommodate Lu at high
477 pressure. This change in Lu incorporation is likely to strongly affect the partitioning
478 of Lu at depth, as is the increased stiffness of magmas at high pressures.

479 Overall these results indicate that not only composition but also pressure induces
480 structural changes in the melt that underpin drastic changes in REE partitioning, and
481 subsequently cause distinct changes in the predicted Lu/Hf ratios from deep magmas.
482 As the melt structure changes with pressure, using a single melt term to normalise the
483 effects of melt on trace element partitioning will not accurately predict partitioning
484 behaviour at depth during magma formation or differentiation. In order to fully under-
485 stand how partitioning is affected by melt structural changes, standard models should

486 be implemented with detailed insight into the exact geometry and elasticity of the REE
487 sites within the melt network with varying pressure.

488 **6. Acknowledgements**

489 C.D.G. was supported by EPSRC for PhD studentship funding with the Condensed
490 Matter Doctoral Training Centre (CM-CDT) under grant number EP/G03673X/1. We
491 thank Diamond Light Source for access to beamline I-15 (proposal EE9022-1) that
492 contributed to some of the results presented here. Portions of this work were performed
493 at HPCAT (Sector 16), Advanced Photon Source (APS), Argonne National Laboratory.
494 HPCAT operations are supported by DOE-NNSA under Award No. DE-NA0001974
495 and DOE-BES under Award No. DE-FG02-99ER45775, with partial instrumentation
496 funding by NSF. The Advanced Photon Source is a U.S. Department of Energy (DOE)
497 Office of Science User Facility operated for the DOE Office of Science by Argonne
498 National Laboratory under Contract No. DE-AC02-06CH11357. We thank N. Guignot
499 on PSICHE beamline at Soleil and Z. Konôpková on P02.2 at PETRAIII. This work
500 was supported by the European Research Council under the European Community's
501 Seventh Framework Programme (FP7/20072013 Grant Agreement No. 259649 to C.
502 Sanloup). We thank G. Bromiley for his help in proofreading this manuscript.

503 **7. References**

- 504 Anderson, A. J., Yan, H., Mayanovic, R. A., Solferino, G., Benmore, C. J., 2014. High-
505 energy X-ray diffraction of a hydrous silicate liquid under conditions of high pressure
506 and temperature in a modified hydrothermal diamond anvil cell. *High Press. Res.*
507 34 (1), 100–109.
- 508 Beattie, P., 1993. On the occurrence of apparent non-Henry’s law behaviour in experi-
509 mental partitioning studies. *Geochim. Cosmochim. Acta* 57, 47–55.
- 510 Benmore, C. J., Soignard, E., Amin, S. A., Guthrie, M., Shastri, S. D., Lee, P. L.,
511 Yarger, J. L., 2010. Structural and topological changes in silica glass at pressure.
512 *Phys. Rev. B* 81, 054105.
- 513 Blundy, J., Wood, B. J., 1994. Prediction of crystal-melt partition coefficients from
514 elastic moduli. *Nature* 372, 452–454.
- 515 Corgne, A., Armstrong, L. S., Keshav, S., Fei, Y., McDonough, W. F., Minarik, W. G.,
516 Moreno, K., 2012. Trace element partitioning between majoritic garnet and silicate
517 melt at 10-17 GPa: Implications for deep mantle processes. *Lithos* 148, 128–141.
- 518 Cottrell, E., Walter, M. J., Walker, D., 2009. Metal-silicate partitioning of tungsten at
519 high pressure and temperature: Implications for equilibrium core formation in Earth.
520 *Earth Planet. Sci. Lett.* 281, 275–287.
- 521 Crépeisson, C., Morard, G., Bureau, H., Prouteau, G., Morizet, Y., Petitgirard, S.,
522 Sanloup, C., 2014. Magmas trapped at depth and the continental lithosphere-
523 asthenosphere boundary. *Earth Planet. Sci. Lett.* 393, 105–112.
- 524 Dingwell, D. B., 1998. The glass transition in hydrous granitic melts. *Phys. Earth*
525 *Planet. Int.* 107, 1–8.
- 526 Draper, D. S., Xirouchakis, D., Agee, C. B., 2003. Trace element partitioning between
527 garnet and chondritic melt from 5 to 9 GPa: implications for the onset of the majorite
528 transition in the martian mantle. *Phys. Earth Planet. Int.* 139, 149–169.
- 529 Drewitt, J. W. E., Jahn, S., Sanloup, C., de Grouchy, C., Garbarino, G., Hennet, L.,
530 2015. Development of chemical and topological structure in aluminosilicate liquids
531 and glasses at high pressure. *J. Phys.: Cond. Matt.* 27, 105103.

- 532 Drewitt, J. W. E., Sanloup, C., Bytchkov, A., Brassamin, S., Hennem, L., 2013. Struc-
533 ture of $(\text{Fe}_x\text{Ca}_{1-x}\text{O})_y(\text{SiO}_2)_{1-y}$ liquids and glasses from high-energy x-ray diffraction:
534 Implications for the structure of natural basaltic magmas. *Phys. Rev. B* 87, 224201.
- 535 Evans, T. M., O'Neill, H. S. C., Tuff, J., 2008. The influence of melt composition on
536 the partitioning of REEs, Y, Sc, Zr and Al between forsterite and melt in the system
537 CMAS. *Geochim. Cosmochim. Acta* 72 (23), 5708–5721.
- 538 Faber, T., Ziman, J., 1965. A theory of the electrical properties of liquid metals. *Philos.*
539 *Mag.* 11, 153–173.
- 540 Farges, F., 1996. Does Zr-F ‘complexation’ occur in magmas? *Chem. Geol* 127 (4),
541 253–268.
- 542 Fei, Y., Mao, H., 1994. In situ determination of the NiAs phase of FeO at high pressure
543 and temperature. *Science* 266 (5191), 1678–1680.
- 544 Funamori, N., Yamamoto, S., Yagi, T., Kikegawa, T., 2004. Exploratory studies of
545 silicate melt structure at high pressures and temperatures by in situ X-ray diffraction.
546 *J. Geophys. Res.* 109, B03203.
- 547 Gaetani, G., 2004. The influence of melt structure on trace element partitioning near
548 the peridotite solidus. *Contrib. Mineral. Petrol.* 147 (5), 511–527.
- 549 Guillot, B., Sator, N., 2007a. A computer simulation study of natural silicate melts.
550 Part I: low pressure properties. *Geochim. Cosmochim. Acta* 71, 1249–1265.
- 551 Guillot, B., Sator, N., 2007b. A computer simulation study of natural silicate melts.
552 Part II: High pressure properties. *Geochim. Cosmochim. Acta* 71, 4538–4556.
- 553 Guitreau, M., Blichert-Toft, J., Martin, J., Mojszisz, S., Albarède, F., 2012. Hafnium
554 isotope evidence from Archean granitic rocks for deep mantle origin of continental
555 crust. *Earth Planet. Sci. Lett.* 337, 211–213.
- 556 Haigis, V., Salanne, M., Simon, S., Wilke, M., Jahn, S., 2013. Molecular dynamics
557 simulations of Y in silicate melts and implications for trace element partitioning.
558 *Chem. Geol.* 346 (SI), 14–21.
- 559 Hajdu, F., 1972. Revised parameters of the analytic fits for coherent and incoherent
560 scattered x-ray intensities of the first 36 atoms. *Acta Cryst.*, 250–252.

- 561 Hammersley, A., 1996. Fit2D. ESRF publication No ESRF98HA01T.
- 562 Hart, S. R., Davis, K. E., 1978. Nickel partitioning between olivine and silicate melt.
563 Earth Planet. Sci. Lett. 40, 203–219.
- 564 Holtz, F., Pichavant, M., Barbey, P., Johannes, W., 1992. Effects of H₂O on liquidus
565 phase relations in the haplogranite system at 2 and 5 kbar . Am. Mineral. 77 (11-12),
566 1223–1241.
- 567 Hosemann, R., Bagchi, S. N., 1962. Direct Analysis of Diffraction by Matter. North-
568 Holland, Amsterdam.
- 569 Hubbell, J. H., Veigele, W. J., Briggs, E. A., Brown, R. T., Cromer, D. T., Hower-
570 ton, R. J., 1975. Atomic form factors, incoherent scattering functions, and photon
571 scattering cross sections. J. Phys. Chem. Ref. Data 4, 471.
- 572 Imai, T., Takahashi, E., Suzuki, T., Hirata, T., 2012. Element partitioning between
573 olivine and melt up to 10 GPa: Implications for the effect of pressure. Phys. Earth
574 Planet. Int. 212, 64–75.
- 575 Kegler, P., Holzheid, A., Frost, D. J., Rubie, D. C., Dohmen, R., Palme, H., 2008. New
576 Ni and Co metal-silicate partitioning data and their relevance for an early terrestrial
577 magma ocean. Earth Planet. Sci. Lett. 268, 28–40.
- 578 Keppler, H., Rubie, D. C., 1993. Pressure-induced coordination changes of transition-
579 metal ions in silicate melts. Nature 364, 54–56.
- 580 Kohara, S., Akola, J., Morita, H., Suzuya, K., Weber, J. K. R., Wilding, M. C., Ben-
581 more, C. J., 2011. Relationship between topological order and glass forming ability in
582 densely packed enstatite and forsterite composition glasses. P. Natl. Acad. Sci. 108,
583 14780–14785.
- 584 Kono, Y., Irifune, T., Higo, Y., Inoue, T., Barnhoorn, A., 2010. P-V-T relation of MgO
585 derived by simultaneous elastic wave velocity and in situ x-ray measurements: A new
586 pressure scale for the mantle transition region. Phys. Earth Planet. Int. 183, 196–211.
- 587 Kono, Y., Park, C., Kenney-Benson, C., Shen, G., Wang, Y., 2014. Toward comprehen-
588 sive studies of liquids at high pressures and high temperatures: Combined structure,
589 elastic wave velocity, and viscosity measurements in the Paris-Edinburgh cell. Phys.
590 Earth Planet. Int. 228, 269–280.

- 591 McIntire, W., 1963. Trace element partitioning coefficients - a review of theory and
592 applications to geology. *Geochim. Cosmochim. Acta* 27, 1209–1264.
- 593 Meade, C., Hemley, R. J., Mao, H. K., 1992. High-pressure x-ray diffraction of SiO₂
594 glass. *Phys. Rev. Lett.* 69, 1387–1390.
- 595 Mysen, B. O., Virgo, D., Harrison, W., Scarfe, C., 1980. Solubility mechanisms of H₂O
596 in silicate melts at high pressures and temperatures: a Raman spectroscopic study.
597 *Am. Miner.* 65, 900–914.
- 598 Ponader, C., Brown, G., 1989. Rare earth elements in silicate glass/melt systems: I.
599 effects of composition on the coordination environments of La, Gd, and Yb. *Geochim.*
600 *Cosmochim. Acta* 53, 2893–2903.
- 601 Prowatke, S., Klemme, S., 2005. Effect of melt composition on the partitioning of trace
602 elements between titanite and silicate melts. *Geochim. Cosmochim. Acta* 69, 695–709.
- 603 Prowatke, S., Klemme, S., 2006. Rare earth element partitioning between titanite and
604 silicate melts: Henry's law revisited. *Geochim. Cosmochim. Acta* 70, 4997–5012.
- 605 Ryerson, F., Hess, P., 1978. Implications of liquid-liquid distribution coefficients to
606 mineral-liquid partitioning. *Geochim. Cosmochim. Acta* 42, 921–932.
- 607 Salters, V., Longhi, J., Bizimis, M., 2002. Near mantle solidus trace element partitioning
608 at pressures up to 3.4 GPa. *G³* 3.
- 609 Salters, V. J. M., Longhi, J., 1999. Trace element partitioning during the initial stages
610 of melting beneath mid-ocean ridges. *Earth Planet. Sci. Lett.* 166, 15–30.
- 611 Sanloup, C., JUL 1 2016. Density of magmas at depth. *Chem. Geol.* 429, 51–59.
- 612 Sanloup, C., Drewitt, J. W. E., Konôpková, Z., Dalladay-Simpson, P., Morton, D. M.,
613 Rai, N., van Westrenen, W., Morgenroth, W., 2013. Structural change in molten
614 basalt at deep mantle conditions. *Nature* 503, 104–107.
- 615 Sanloup, C., van Westrenen, W., Dasgupta, R., Maynard-Casely, H. E., Perrillat, J.-P.,
616 2011. Compressibility change in iron-rich melt and implications for core formation
617 models. *Earth Planet. Sci. Lett.* 306, 118–122.

- 618 Sato, T., Funamori, N., 2010. High-pressure structural transformation of SiO₂ glass up
619 to 100 GPa. *Phys. Rev. B* 82, 184102.
- 620 Schmidt, M. W., Connolly, J. A. D., Gunther, D., Bogaerts, M., 2006. Element parti-
621 tioning: The role of melt structure and composition. *Nature* 312, 1646–1650.
- 622 Shannon, R. D., 1976. Revised effective ionic radii and systematic studies of interatomic
623 distances in halides and chalcogenides. *Acta Crystallogr.*, 751–767.
- 624 Simon, S., Wilke, M., Chernikov, R., Klemme, S., Hennet, L., 2013. The influence
625 of composition on the local structure around yttrium in quenched silicate melts -
626 insights from EXAFS. *Chem. Geol.* 346, 3–13.
- 627 Sun, N., Stixrude, L., de Koker, N., Karki, B. B., 2011. First principles molecular
628 dynamics simulations of diopside (CaMgSi₂O₆) liquid to high pressure. *Geochim.*
629 *Cosmochim. Acta* 75, 3792–3802.
- 630 Suzuki, T., Hirata, T., Yokoyama, T. D., Imai, T., Takahashi, E., 2012. Pressure effect
631 on element partitioning between minerals and silicate melt: Melting experiments on
632 basalt up to 20 GPa. *Phys. Earth Planet. Int.* 208, 59–73.
- 633 Uhlig, H., Hoffmann, M. J., Lamparter, P., Steeb, S., 1998. Atomic structure of rare
634 earth Si-Al-O-N glasses. *Z. Naturforsch.* 53, 259–264.
- 635 van Westrenen, W., Allan, N. L., Blundy, J. D., Purton, J. A., Wood, B. J., 2000.
636 Atomistic simulation of trace element incorporation into garnets — comparison with
637 experimental garnet-melt partitioning data. *Geochim. Cosmochim. Acta* 64, 1629–
638 1639.
- 639 van Westrenen, W., Draper, D. S., 2007. Quantifying garnet-melt trace element parti-
640 tioning using lattice-strain theory: new crystal-chemical and thermodynamic con-
641 straints. *Contrib. Mineral. Petrol.* 154 (6), 717–730.
- 642 van Westrenen, W., Wood, B. J., Blundy, J., 1999. Crystal-chemistry controls on trace
643 element partitioning between garnet and anhydrous silicate melts. *Am. Mineral.* 84,
644 838–847.
- 645 Vuilleumier, R., Sator, N., Guillot, B., 2009. Computer modeling of natural silicate
646 melts: What can we learn from ab initio simulations. *Geochim. Cosmochim. Acta* 73,
647 6313–6339.

- 648 Wang, Y. B., Sakamaki, T., Skinner, L. B., Jing, Z., Yu, T., Kono, Y., Park, C., Shen,
649 G., Rivers, M. L., Sutton, S. R., 2014. Atomistic insight into viscosity and density of
650 silicate melts under pressure. *Nature Comm.* 5, 3241.
- 651 Wood, B., Blundy, J., 1997. A predictive model for rare earth element partitioning
652 between clinopyroxene and anhydrous silicate melt. *Contrib. Mineral. Petrol.* 129 (2-
653 3), 166–181.
- 654 Wood, B. J., Blundy, J. D., 2013. Trace Element Partitioning : The Influences of Ionic
655 Radius, Cation Charge, Pressure, and Temperature. Vol. 437. JAI-Elsevier Science
656 inc., pp. 421–448.
- 657 Yamada, A., Inoue, T., Urakawa, S., Funakoshi, K.-i., Funamori, N., Kikegawa, T.,
658 Ohfuji, H., Irifune, T., 2007. In situ X-ray experiment on the structure of hydrous
659 Mg-silicate melt under high pressure and high temperature. *Geophys. Res. Lett.*
660 34 (10).
- 661 Yarger, J. L., Smith, K. H., Nieman, R. A., Diefenbacher, J., Wolf, G. H., Poe, B. T.,
662 McMillan, P. F., 1995. Al coordination changes in high-pressure aluminosilicate liq-
663 uids. *Science* 270, 1964–1967.
- 664 Zeidler, A., Drewitt, J. W. E., Salmon, P. S., Barnes, A. C., Crichton, W. A., Klotz,
665 S., Fischer, H. E., Benmore, C. J., Ramos, S., Hannon, A. C., 2009. Establishing the
666 structure of GeS₂ at high pressures and temperatures: a combined approach using
667 x-ray and neutron diffraction. *J. Phys. Cond. Matt.* 21 (47).